LocRa: Enable Practical Long-Range Backscatter Localization for Low-Cost Tags

Jinyan Jiang, Jiliang Wang, Yijie Chen, Yihao Liu, Yunhao Liu
Tsinghua University, Beijing, P.R. China
jiangjy20@mails.tsinghua.edu.cn, jiliangwang@tsinghua.edu.cn, {cyj20, liuyihao18}@mails.tsinghua.edu.cn,
yunhao@tsinghua.edu.cn

ABSTRACT

Long-range backscatter localization is a promising technology for the Internet of Things. Existing works cannot work well for distributed base stations and low-cost tags. We present LocRa, which provides accurate localization for long-range backscatter with distributed base stations. We present a novel method to extract accurate channel information and synchronize the phase of different base stations. To compensate for the frequency and phase error on low-cost tags, we combine multiple channel measurements and eliminate the error by aligning different channels. Finally, we exploit frequency domain characteristics of the backscatter signal to extend its bandwidth and improve the SNR, thereby enhancing the localization accuracy. We prototype LocRa tags using custom low-cost hardware and implement LocRa base stations on USRP. Through extensive experiments, we show that the localization error of LocRa is 6.8 cm and 88 cm when the tag is 5 m and 50 m away from the base station, which is 3.1× and 2.3× better than the state-of-the-arts methods.

CCS CONCEPTS

• **Information systems** → **Sensor networks**; **Global positioning systems**; • **Networks** → **Cyber-physical networks**.

KEYWORDS

Backscatter, Wireless Localization, LoRa

ACM Reference Format:
Jinyan Jiang, Jiliang Wang, Yijie Chen, Yihao Liu, Yunhao Liu. 2023. LocRa: Enable Practical Long-Range Backscatter Localization for Low-Cost Tags. In *The 21st Annual International Conference on Mobile Systems, Applications and Services (MobiSys '23), June 18–22, 2023, Helsinki, Finland.* ACM, New York, NY, USA, 13 pages. https://doi.org/10.1145/3581791.3596863

1 INTRODUCTION

Recent advances in wireless localization enable various new applications in the Internet of Things (IoT), such as smart homes, smart agriculture, and smart healthcare [1–13]. Backscatter localization systems have brought smaller form factors and lower power consumption to wireless localization. More specifically, the recent development of long-range backscatter [8, 13–16] (e.g., LoRa backscatter) is considered to be promising as it significantly extends the communication and localization range. However, existing long-range backscatter localization systems still face the following key challenges while applying to practical scenarios:

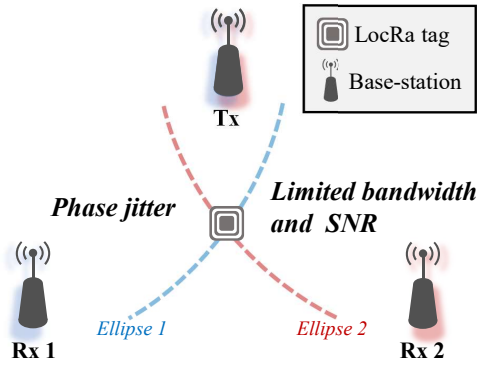

Figure 1: LocRa provides long-range backscatter localization for low-cost tags with distributed base stations.

Distributed base stations. Backscatter localization systems usually require the time/phase synchornization between transmitters (Tx) and receivers (Rx) to calculate the Time-of-Flight (ToF). To achieve precise synchornization among transceivers, some past works [8, 13, 17] exploit a common external reference clock shared through RF cables. However, it is not practical for distributed base stations because deploying such long cables is high-cost and inconvenient in practice. For wireless synchronization techniques, such as GPSDO [18] and RFclock [19], they need to add extra hardware to existing base stations. Moreover, the effectiveness of these solutions is significantly degraded in indoor multipath environments [20].

Low-cost backscatter tags. The unstable low-cost and low-power oscillators on backscatter tags cause severe frequency and phase error in backscatter signal, which reduces the localization accuracy. External environmental factors (e.g., temperature, humidity and pressure [21]) further worsen the error. Previous works, *e.g.*, μlocate, propose to measure the shifting frequency of tags and then use it to calibrate the phase shift. However, it is difficult to accurately measure the unstable shifting frequency in a multipath environment (details in §4).

Low SNR backscatter signal of limited bandwidth. The backscatter signal usually has a very low SNR and limited bandwidth, especially in long-range localization (e.g., LoRa backscatter). Traditional

MobiSys '23, June 18–22, 2023, Helsinki, Finland

ACM ISBN 979-8-4007-0110-8/23/06.
https://doi.org/10.1145/3581791.3596863

approaches need to increase the power and duration of the excitation signal and use a larger bandwidth to improve the localization accuracy. However, this increases the cost and delay for backscatter localization. It also cannot work for long-range backscatter networks of LoRa with a very low SNR and limited bandwidth (details in §5).

To address the above challenges and make long-range backscatter localization work in practice, we present *LocRa*, the first **Loc**alization system for Long-**Ra**nge backscatter tags with distributed base stations. As shown in Fig. 1, LocRa can work for unsynchronized single-antenna base stations, e.g., one LoRa base station as the Tx and another as the Rx, and thus use existing network as the infrastructure. The LocRa tag, as in many other backscatter systems [8, 22–30], shifts the frequency of the excitation signal using low-cost and lower-power oscillators. LocRa accurately calculates the travel time of the backscatter signal and the total travel distance for the backscatter signal. By combining the distance to different base stations, LocRa can provide the localization of the backscatter tag. In the design of LocRa, we address the following key problems:

(1) How to address the random phase shift between Tx and Rx? The random phase shift introduced during up-/down-converting in Tx and Rx (details explained in § 2) results in a large localization error. Since the excitation and backscatter signals should experience the same frequency and phase offset, we leverage the excitation signal to correct the phase shift of the backscatter signal. To obtain the phase shift of the excitation signal, a naive approach is to use the location of base stations to infer the channel. But this method suffers from severe distortion in real multipath environment. Existing works can measure the channel between two transceivers based on the excitation signal [3]. However, we show that they lead to too many degrees of freedom and thus cannot work well in practice, causing ambiguity in phase shift estimation. We propose a novel method to effectively and accurately measure the channel between base stations and resolve the ambiguity in phase estimation.

(2) How to address phase error in unstable backscatter tags? The frequency and initial phase of the backscatter signal drift over time due to the low-power, high-jitter crystal oscillator on the tag, resulting in localization failure. In § 4, we build three types of tags using different crystal oscillators and demonstrate the phase error for the backscatter signal. To address this, the key idea is that the phase of the same channel at the same frequency is expected to be the same. Therefore, we propose a method to continuously calibrate the channel phase by combining multiple measurements at the same frequency and then eliminate the initial drifting phase of the backscatter signal. During the whole calibration process, backscatter tags only need to shift the frequency. All the parameter selection and channel calculation operations are performed at the base stations.

(3) How to improve localization accuracy for low-SNR backscatter signal of limited bandwidth? The backscatter signal is typically weak and heavily distorted, making it difficult to extract localization information from it. To address this, we use LoRa signal as the excitation signal, which allows to concentrate the energy of the backscatter signal in the time domain and extract the channel state information (CSI) in the frequency domain. Moreover, the backscatter signal can be decomposed into multiple sidebands in the frequency domain, *i.e.,* the upper and lower sidebands. Previous works only use one of the sidebands. Combining multiple sidebands can improve the signal bandwidth and SNR. However, directly combining sidebands cannot work due to the unmatched initial phase and frequency discontinuity in the spectrum. By analyzing the characteristics of the upper and lower sidebands, we propose a method to combine double-sidebands signal to extend the bandwidth and increase the signal SNR, thereby improving the localization accuracy.

Main results and contributions.

- We investigate the key limitations for long-range backscatter localization systems with distributed base stations and low-cost tags. We show that those limitations lead to significant localization error and existing works cannot effectively address them.
- We propose LocRa, a long-range backscatter localization system with distributed base stations and low-cost tags. We design a method to eliminate the frequency and phase offset between distributed unsynchronized base stations and resolve the ambiguity in existing works. We propose a method to calibrate the output phase of backscatter tags with low-cost and low-power crystal oscillators. Finally, we leverage double sidebands of the backscatter signal to improve the signal bandwidth and SNR, and thus improve localization accuracy.
- We implement LocRa tag on a customized PCB board using commercial low-cost and low-power off-the-shelf components. The evaluation results show that the localization error of LocRa is 6.8 cm and 88 cm when the tag is 5 m and 50 m away from the base station; compared with the state-of-the-arts, LocRa achieves 3.1× and 2.3× higher localization accuracy.

2 LOCALIZATION MODEL

There are three main parts of LocRa, as shown in Fig. 2. The Tx (e.g., a LoRa base station) sends a LoRa chirp. The signal is frequency shifted by a LocRa tag and then received by the Rx (e.g., another LoRa base station). Based on the received excitation and backscatter chirp, the Rx derives the location of the tag. The Tx and Rx can be far from each other, and there is no synchronization cable between Tx and Rx.

The Tx first generates a signal in the baseband, as shown in Fig. 2(a). We take a LoRa base up-chirp $s(t) = e^{j2\pi(f_0 t + \frac{1}{2}kt^2)}$ as an example, where f_0 is the starting frequency, and k is the frequency changing rate. The Tx then up-converts the baseband signal to $S(t)$ using a high-frequency carrier signal:

$$S(t) = s(t) \cdot e^{j(2\pi f_c t + \theta_{Tx})} \tag{1}$$

where f_c and θ_{Tx} are the frequency and initial phase of the carrier.

Then, the signal experiences various reflections through different paths. For a backscatter tag, assume there are m different paths between Tx and Tag with attenuation $\{\alpha_1^1, \alpha_1^2, \ldots, \alpha_1^m\}$ and delay $\{\tau_1^1, \tau_1^2, \ldots, \tau_1^m\}$, and there are n paths between Tag and Rx with attenuation $\{\alpha_2^1, \alpha_2^2, \ldots, \alpha_2^n\}$ and delay $\{\tau_2^1, \tau_2^2, \ldots, \tau_2^n\}$. As a result, the received backscatter signal consists of $m \cdot n$ multipaths, which is a pairwise combination of the Tx-to-Tag path and Tag-to-Rx path. We first analyze one signal path of τ_1^i and τ_2^k, then extend it to the multipath case.

As shown in Fig. 2(b), the tag shifts the frequency of the incoming signal by $e^{j(2\pi\Delta f t + \theta_{Tag})}$, where Δf is the shifted frequency and

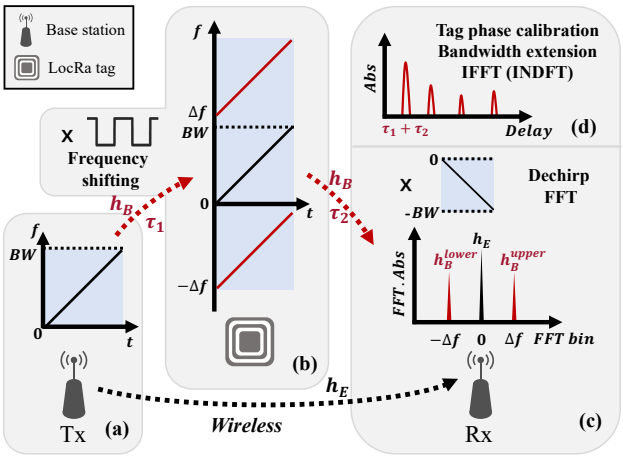

Figure 2: The main workflow of LocRa.

θ_{Tag} is the initial phase. The backscatter signal $S_B(t)$ is

$$S_B(t) = \alpha_1^i \cdot s(t-\tau_1^i) \cdot e^{j(2\pi f_c(t-\tau_1^i)+\theta_{Tx})} \cdot e^{j(2\pi\Delta f t+\theta_{Tag})} \tag{2}$$

The backscatter signal then propagates with time τ_2^k and attenuation α_2^k. Thus, Rx receives the backscatter signal $R_B(t)$:

$$\begin{aligned} R_B(t) =& \alpha_2^k \cdot S_B(t-\tau_2^k) \\ =& \alpha_1^i\alpha_2^k \cdot s(t-\tau_1^i-\tau_2^k) \cdot e^{j(2\pi f_c(t-\tau_1^i-\tau_2^k)+\theta_{Tx})} \\ & \cdot e^{j(2\pi\Delta f(t-\tau_2^k)+\theta_{Tag})} \end{aligned} \tag{3}$$

Then, Rx down-converts the signal $R_B(t)$ to the baseband $r_B(t)$ using negative carrier signal $e^{-j(2\pi f_c'+\theta_{Rx})}$, where f_c' and θ_{Rx} are the frequency and initial phase of the carrier. Since Tx and Rx are not synchronized, Rx has a time offset γ in the sampling window to process the baseband signal:

$$\begin{aligned} r_B(t+\gamma) =& \alpha_1^i\alpha_2^k \cdot s(t+\gamma-\tau_1^i-\tau_2^k) \cdot e^{j2\pi\cdot f_{CFO}\cdot(t+\gamma)} \\ & \cdot e^{-j2\pi f_c(\tau_1^i+\tau_2^k)} \cdot e^{j(\theta_{Tx}-\theta_{Rx})} \cdot e^{j(2\pi\Delta f(t+\gamma-\tau_2^k)+\theta_{Tag})} \\ \approx& \alpha_1^i\alpha_2^k \cdot s(t) \cdot e^{j2\pi\cdot f_{CFO}\cdot(t+\gamma)} \cdot e^{-j2\pi f_c(\tau_1^i+\tau_2^k)} \\ & \cdot e^{j(\theta_{Tx}-\theta_{Rx})} \cdot e^{j(2\pi\Delta f(t+\gamma-\tau_2^k)+\theta_{Tag})} \end{aligned} \tag{4}$$

where $f_{CFO} = f_c - f_c'$. Without loss of generality, we set the starting frequency f_0 of the chirp signal $s(t)$ as 0 and then ignore γ and τ in $s(t-\gamma-\tau_1^i-\tau_2^k)$ as the quadratic term of this tiny delay has little effect on the result.

To obtain the channel state information, we first *dechirp* the received chirp symbol $r_B(t+\gamma)$, *i.e.,* multiply it with a down-chirp $s^*(t)$ (the conjugate of a base up-chirp). Then, we apply FFT to the dechirp results and calculate the peak of backscatter signal in the frequency domain (shown as the red peak in Fig. 2(c)). The value of the corresponding FFT bin $\hat{h_B}(f_c)$ is

$$\begin{aligned} \hat{h_B}(f_c) =& \alpha_1^i\alpha_2^k e^{-j2\pi\Delta f\tau_2^k} \cdot e^{-j2\pi f_c(\tau_1^i+\tau_2^k)} \cdot e^{-j2\pi\cdot f_{CFO}\cdot\gamma} \\ & \cdot e^{j(\theta_{Tx}-\theta_{Rx})} \cdot e^{j\Theta_{Tag}} \\ =& h_B(f_c) \cdot e^{j2\pi\cdot f_{CFO}\cdot\gamma} \cdot e^{j(\theta_{Tx}-\theta_{Rx})} \cdot e^{j\Theta_{Tag}} \end{aligned} \tag{5}$$

where $h_B(f_c) = \alpha_1^i\alpha_2^k e^{-j2\pi\Delta f\tau_2^k} \cdot e^{-j2\pi f_c(\tau_1^i+\tau_2^k)}$ is the real channel of the backscatter signal, $\Theta_{Tag} = \theta_{tag} + 2\pi\Delta f\gamma$ is the phase error introduced by the tag and γ is the sampling window offset. Note that the term $e^{-j2\pi\Delta f\tau_2^k}$ remains the same across different carrier frequencies, indicating that the channel has a fixed phase rotation.

We can extend the channel $h_B(f_c)$ for a signal path to $m \cdot n$ paths as

$$h_B(f_c) = \sum_{i=1}^{m}\sum_{k=1}^{n} A_{i,k} \cdot e^{-j2\pi f_c T_{i,k}} \tag{6}$$

where $A_{i,k} = \alpha_1^i\alpha_2^k e^{-j2\pi\Delta f\tau_2^k}$ and $T_{i,k} = \tau_1^i + \tau_2^k$.

Assume τ_1^1 and τ_2^1 are the delays for the LoS Tx-Tag and Tag-Rx path, respectively. We need to calculate $T_{1,1} = \tau_1^1 + \tau_2^1$ for localization. By measuring the channel at multiple carrier frequencies f_c and performing IFFT operation on the channel value sequence, we can calculate the Channel Impulse Response (CIR) $f(t)$:

$$f_B(t) = \sum_{i=1}^{m}\sum_{k=1}^{n} A_{i,k} \cdot \delta(t-T_{i,k}) \tag{7}$$

where $\delta(\cdot)$ is the delta function, as shown in Fig. 2(d). Eq. 7 describes the attenuation ($A_{i,k}$) and delay ($T_{i,k}$) of each path. We calculate the travel time $T_{1,1}$ for the LoS path from the first impulse $\delta(t-T_{1,1})$ and then calculate the sum of Tx-to-Tag and Tag-to-Rx distance. We can determine an ellipse based on the location of the Tx and Rx. With multiple Rxs, we can use the intersection of ellipses as the tag location. We need at least two Rxs to determine two ellipses.

2.1 Challenges

Frequency and phase misalignment between Tx and Rx. In Eq. 5, the frequency and phase offset between Tx and Rx, *i.e.,* $e^{j2\pi\cdot f_{CFO}\gamma}$ and $e^{j(\theta_{Tx}-\theta_{Rx})}$, introduce error to the channel estimation of $h_B(f_c)$. For different frequency f_c, the local oscillators in Tx and Rx will output a random initial phase θ_{Tx} and θ_{Rx} for the carrier. The f_{CFO} is also different for different center frequency f_c. Although channel estimation between static transceivers has been a well-studied topic in wireless communicaiton [31, 32], they cannot work in our scenario as we need to decouple the phase shift from CFO and other factors. To address this, μlocate [8] exploits an external clock connected with both Tx and Rx to provide a reference clock to cancel the f_{CFO} between Tx and Rx. This also provides identical θ_{Tx} and θ_{Rx}. GPSDO [18] can use the GPS satellite broadcast signal to synchronize the time and phase of each transceiver outdoors. RFclock [19] designs an external board for SDRs to share a common reference clock. Chronos [3] requires Tx and Rx to exchange a packet to calibrate the frequency and phase offset. However, Chronos cannot provide accurate multipath information for localization (details in § 3.2).

Tag phase error. In Eq. 5, there is another error term $e^{j\Theta_{Tag}}$ introduced by the tag. As shown in Fig. 3, suppose Tx sends the excitation chirp of length ΔT at three different carrier frequencies.

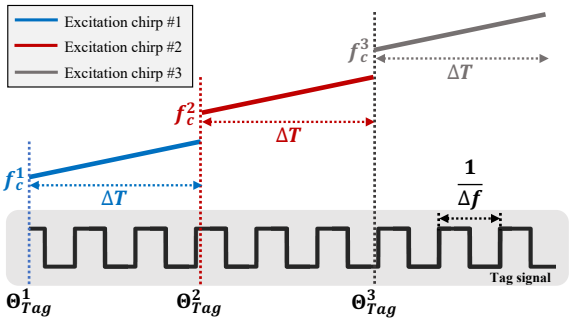

Figure 3: The phase of the backscatter signal varies over time, affecting the channel measurement at different carrier frequencies.

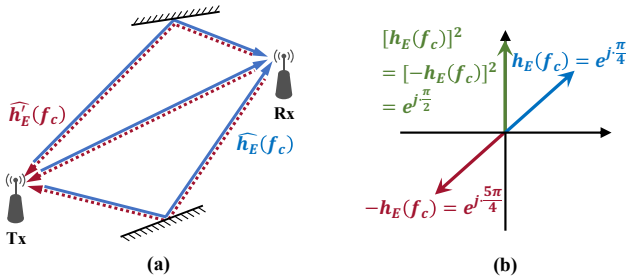

Figure 4: (a) The phase mismatch between Tx and Rx can be eliminated by exchanging data packets between them. (b) The green vector $h_E(f_c)^2$ corresponds to two possible $h_E(f_c)$, shown as the red and blue vectors.

The tag uses a single frequency signal $e^{j(2\pi\Delta f t+\Theta_{Tag})}$ to shift the excitation chirp. It introduces three different initial phases (Θ_{Tag}^1, Θ_{Tag}^2, and Θ_{Tag}^3) to the three excitation chirps. For localization, we need to remove this phase error. A naive approach is to make the tag output the same phase at the beginning of each excitation chirp. However, this requires the tag and Tx are strictly synchronized, which is difficult for low power tags. Theoretically, those three phases are related, *e.g.*, , $\Theta_{Tag}^2 = \Theta_{Tag}^1 + 2\pi\Delta f\Delta T$. We can measure the shifting frequency Δf and then obtain the phase offset at different time. However, this requires that the output frequency of the tag is stable and can be accurately measured, which is difficult for low-power tags to transmit signals in a multipath environment (details in § 4.1). For synchronized Tx and Rx, multiple simultaneous backscatter signals can be used to remove the phase error [8]. However, the simultaneous data flow reduces the transmission power and affects the communication distance. In §4, we implement tags with oscillators of different prices and power consumption. We find that this error for high-priced precision tags is negligible. But for low-power and low-cost tags, it is challenging to make them work in practice.

Low bandwidth and SNR. The localization accuracy in Eq. 7 depends on the accuracy of the time impulse. From Eq. 6 to Eq. 7, two factors affect the IFFT operation: signal bandwidth and SNR. The resolution of the time impulse is $1/B$, where B is the total bandwidth. Thus, a higher bandwidth B improves the localization accuracy. This, however, occupies more wireless spectrums and increases the localization delay. Besides, the backscatter signal is typically very weak and is easily distorted by the noise, which affects the accuracy of the time-domain impulse. We leverage a unique characteristic of the backscatter signal to expand the bandwidth and thus enhance the localization accuracy (§ 5).

3 SEPARATION OF TX AND RX

To separate Tx and Rx, we need to eliminate the random phase offset of each channel measurement. We notice that Rx receives both the backscatter signal and the excitation signal. We can use the channel measurement of the excitation signal to calibrate that of the backscatter signal.

3.1 Calibration with Excitation Signal

Both the backscatter signal and the excitation signal are generated by the same Tx and are sampled simultaneously. Thus, they share the same phase offset. We apply channel measurement to the excitation signal similar to Eq. 5 to obtain $\hat{h_B}(f_c)$:

$$\hat{h_E}(f_c) = h_E(f_c) \cdot e^{j2\pi \cdot f_{CFO} \cdot \gamma} \cdot e^{j(\theta_{Tx}-\theta_{Rx})} \tag{8}$$

Here, we temporarily ignore the phase offset Θ_{Tag} caused by the tag. By dividing these two measured channel states, we have:

$$\frac{\hat{h_B}(f_c)}{\hat{h_E}(f_c)} = \frac{h_B(f_c) \cdot \cancel{e^{j(\theta_{Tx}-\theta_{Rx})}} \cdot \cancel{e^{j2\pi \cdot f_{CFO} \cdot \gamma}}}{h_E(f_c) \cdot \cancel{e^{j(\theta_{Tx}-\theta_{Rx})}} \cdot \cancel{e^{j2\pi \cdot f_{CFO} \cdot \gamma}}} = \frac{h_B(f_c)}{h_E(f_c)} \tag{9}$$

After canceling the random phase offset, we can obtain the offset-free channel of the backscatter signal $h_B(f_c)$:

$$h_B(f_c) = \frac{\hat{h_B}(f_c)}{\hat{h_E}(f_c)} \cdot h_E(f_c) \tag{10}$$

In Eq. 10, the channel of the excitation signal and backscatter signal (*i.e.*, $\hat{h_B}(f_c)$ and $\hat{h_E}(f_c)$) can be measured. The only unknown term is the offset-free channel measurement of the excitation signal, *i.e.*, $h_E(f_c)$. A naive approximation is to estimate the LoS path of the excitation signal. However, this approach suffers from severe distortion in real multipath environments.

3.2 Measurement of the Excitation Signal

To measure the offset-free channel of the excitation signal h_E, we let the Tx send a packet to Rx, and then the Rx responds one to the Tx as in Chronos [3]. As shown in Fig. 4(a), we have the channel measurement $\hat{h_E}(f_c)$ from Tx to Rx and the inverse channel measurement $\hat{h_E'}(f_c)$ from Rx to Tx:

$$\hat{h_E'}(f_c) = h_E(f_c) \cdot e^{j(\theta_{Rx}-\theta_{Tx})} \cdot e^{-j2\pi \cdot f_{CFO} \cdot \gamma'} \tag{11}$$

Comparing Eq. 8 with 11, both $\hat{h_E}$ and $\hat{h_E'}$ have three main terms: (1) the same h_E in both equations because of channel reciprocity [33]; (2) $e^{j(\theta_{Tx}-\theta_{Rx})}$ and $e^{j(\theta_{Rx}-\theta_{Tx})}$ are conjugated to each other as most transceivers use the same oscillator for transmitting and receiving; (3) $e^{j2\pi \cdot f_{CFO} \cdot \gamma}$ and $e^{-j2\pi \cdot f_{CFO} \cdot \gamma'}$ are similar.

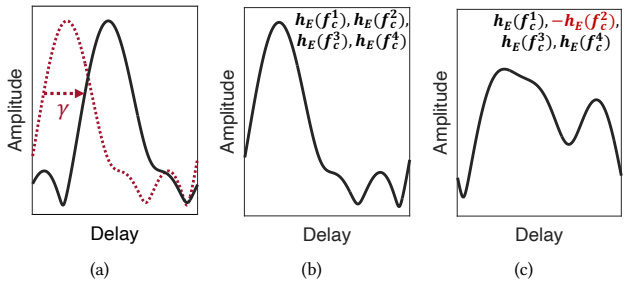

Figure 5: (a) The real CIR and the reference CIR; (b) The correct sequence $\{h_1, h_2, h_3, h_4\}$ results in the CIR with the same waveform as the reference CIR; (c) The wrong sequence $\{h_1, -h_2, h_3, h_4\}$ results in different waveforms.

To cancel the random phase offset $e^{j(\theta_{Tx}-\theta_{Rx})}$ in Eq. 8 and 11, we multiply the original and inverse channel measurement:

$$\begin{aligned}\hat{h_E}(f_c)\cdot\hat{h_E'}(f_c) =& h_E(f_c)\cdot\cancel{e^{j(\theta_{Tx}-\theta_{Rx})}}\cdot e^{j2\pi\cdot f_{CFO}\cdot\gamma}\\ &\cdot h_E(f_c)\cdot\cancel{e^{j(\theta_{Rx}-\theta_{Tx})}}\cdot e^{-j2\pi\cdot f_{CFO}\cdot\gamma'} \\ =& h_E(f_c)^2\cdot e^{j2\pi\cdot f_{CFO}\cdot(\gamma-\gamma')}\end{aligned} \tag{12}$$

In Eq. 12, f_{CFO} between Tx and Rx can be easily estimated by sending a preamble with a known baseband frequency, and $\gamma-\gamma'$ is the time delay between two channel measurements, which can also be measured. We then cancel $e^{j2\pi\cdot f_{CFO}\cdot(\gamma-\gamma')}$ from Eq. 12 and obtain $h_E^2(f_c)$. Existing works take the square root of $h_E(f_c)^2$ to derive $h_E(f_c)$. However, this leads to ambiguous results as the square root of $h_E(f_c)^2$ has two possible solutions: $\sqrt{h_E(f_c)^2} = \pm h_E(f_c)$. In other words, we can have either h or h rotated by phase π, *i.e.,* $-h_E(f_c) = h_E(f_c)\cdot e^{j\pi}$. Fig. 4 shows an example, both $h_E(f_c) = e^{j\cdot\frac{\pi}{4}}$ and $-h_E(f_c) = e^{j\cdot\frac{5\pi}{4}}$ result in $h_E(f_c)^2 = [-h_E(f_c)]^2 = e^{j\cdot\frac{\pi}{2}}$. Our method needs to measure the channel at multiple carrier frequencies (*e.g., p* frequencies) to distinguish the multipath as mentioned in § 2. Therefore, there are 2^p possible values for the channel measurement sequence: $\{\pm h_E(f_c^1), \pm h_E(f_c^2), \ldots, \pm h_E(f_c^p)\}$, each leading to a different localization result. Chronos directly apply IFFT to the sequence of $h_E(f_c)^2$. It increases the number of multipaths and reduces the localization accuracy [3]. We will resolve the ambiguity brought by $h_E(f_c)^2$ in the next subsection, so as to improve the localization performance.

3.3 Ambiguity Resolution

To find the correct one from 2^p possible sequences, we send a signal containing p frequencies:

$$S(t) = \sum_{k=1}^{p} e^{j2\pi f_c^k t}\cdot e^{j\theta_{Tx}} \tag{13}$$

As described in § 2, $S(t)$ is down-converted, sampled by Rx. We set the down-converting frequency to f_c^1. Then, we apply FFT to obtain the channel state at each frequency:

$$\hat{h_E}\left(f_c^i\right) = \sum_{k=1}^{n}\alpha_k' e^{j2\pi f_c^i(-\tau_k+\gamma)} \tag{14}$$

where $\alpha_k' = \alpha_k\cdot e^{j(\theta_{Tx}-\theta_{Rx})}\cdot e^{j2\pi\cdot f_{CFO}\cdot\gamma}\cdot e^{-j2\pi f_c^1\gamma}$. Because of the unsynchronized clock between the Tx and Rx, the sampling window offset γ introduce a phase offset related to the carrier frequency f_c^i. As a result, by applying IFFT on the measured channel sequence, we have the CIR $\hat{f}(t)$:

$$\hat{f_E}(t) = \sum_{k=1}^{n}\alpha_k'\cdot\delta(t-\tau_k+\gamma) \tag{15}$$

We can see from Eq. 15 that (1) compared with the real CIR $f_E(t)$, the position of the measured CIR is shifted by the sampling window offset γ, and (2) the waveform of the measured CIR is the same with that of $f_E(t)$. Therefore, we can leverage the waveform of $\hat{f_E}(t)$ as the *reference CIR* to find out the correct channel estimation sequence.

Fig. 5(a) shows the reference CIR derived from signals with four frequencies. Fig. 5(b) is the CIR of the sequence $\{h_E(f_c^1), h_E(f_c^2), h_E(f_c^3), h_E(f_c^4)\}$. We can see that the waveform of the reference CIR is the same as the real one except with a shifted time offset. As shown in Fig. 5(c), the CIR of the sequence $\{h_E(f_c^1), -h_E(f_c^2), h_E(f_c^3), h_E(f_c^4)\}$ is severely distorted. The reason is that the inversion of $-h_E(f_c^2)$ causes the peaks of the time-domain CIR to interfere with each other, thus distorting the waveform.

To find out the correct sequence among all possible sequences, we take advantage of the reference CIR. We first estimate the reference CIR. Then, we search in every sequences to find the sequence with the same waveform as the reference CIR (*i.e.,* Fig. 5(a)).

Unfortunately, besides the correct sequence $\{h_E(f_c^1), h_E(f_c^2), \ldots, h_E(f_c^p)\}$, three other sequences also have the same waveform with the correct sequence, *i.e.,*

$$\{-h_E(f_c^1), -h_E(f_c^2), \ldots, -h_E(f_c^p)\} \tag{16}$$

$$\{h_E(f_c^1), -h_E(f_c^2), \ldots, h_E(f_c^{2k-1}), -h_E(f_c^{2k}), \ldots\} \tag{17}$$

$$\{-h_E(f_c^1), h_E(f_c^2), \ldots, -h_E(f_c^{2k-1}), h_E(f_c^{2k}), \ldots\} \tag{18}$$

Sequence 16 can be derived by multiplying the real sequence by the same phase, *i.e.,* $e^{j\pi} = -1$, which results in the same time-domain waveform. Each time-domain pulse retains the same position and amplitude but with a different phase. It is equivalent to multiplying the channel of the backscatter signal in Eq. 10 by a fixed phase offset $e^{j\pi}$. As mentioned in § 2, this does not affect the time-domain waveform of the backscatter channel value sequence $f_B(t)$.

For sequence 17, it is equivalent to multiplying the original channel value sequence by a uniformly growing phase sequence: $\{e^{j0\pi}, e^{j1\pi}, e^{j2\pi}, \ldots\}$. As mentioned for Eq. 14, this phase rotation in frequency domain can be transformed to be a offset in time domain. Assuming the difference between two adjacent carrier frequencies is F, we express the channel estimation sequence as:

$$\hat{h_E}\left(f_c^i\right) = \sum_{k=1}^{n}\alpha_k' e^{j2\pi f_c^i(-\tau_k+\frac{1}{2F})} \tag{19}$$

where $\alpha_k' = \alpha_k e^{-j2\pi f_c^1\cdot\frac{1}{2F}}$. By applying IFFT to Eq. 19, similar to what happens in Eq. 15, we have the same time domain waveform with $f_E(t)$ but with a time offset $\frac{1}{2F}$.

Sequence 18 is similar to sequence 17. It is equivalent to multiplying sequence 17 with a fixed phase offset $e^{j\pi}$. As mentioned above, it will not affect the waveform of the time domain impulse.

Thus, it also has the same waveform with $f_E(t)$ but with a time offset $\frac{1}{2F}$.

We can obtain four possible channel sequences with the same waveform as that of the reference CIR. But two of them (Sequences 17 and 18) have a fixed time shift $\frac{1}{2F}$, and should be removed. Note that the first pulse of the CIR, which indicates the LoS delay between Tx and Rx, should be known given the distance between Tx and Rx. Thus, the first pulse of the correct sequence should have the first pulse consistent with the distance between Tx and Rx. As the frequency difference F is less than 5 MHz in our system, the distance shift for sequence 17 is more than $\frac{1}{2 \cdot 5\ MHz} \cdot c = 30$ m, where c is the speed of light. We can leverage this to remove those sequences with the waveform.

Therefore, we can identify the correct sequence by searching in 2^p sequences based on the waveform and time shift. The complexity of this algorithm is $O(2^p)$. To reduce the complexity, we propose an overlapping group based method. We divide the channel estimation sequence into groups of size C, where two adjacent groups have an overlapping frequency. Each group has a constant number of channel estimations. For example, when $p = 7$ and $C = 4$, we can divide the sequence into two groups: $\{f_c^1, f_c^2, f_c^3, f_c^4\}$ and $\{f_c^4, f_c^5, f_c^6, f_c^7\}$. For each group, we can search for the correct sequence. For group # 1, the result can be $\{h_E(f_c^1), h_E(f_c^2), h_E(f_c^3), h_E(f_c^4)\}$ or $\{-h_E(f_c^1), -h_E(f_c^2), -h_E(f_c^3), -h_E(f_c^4)\}$. For group # 2, the situation is similar. By ensuring that the overlapping estimations $h_E(f_c^4)$ in both groups have the same phase, we can combine groups to obtain the whole correct sequence. Thus, the complexity of this algorithm is reduced to $O(p)$. We note that using fewer elements in each group helps to speed up the calculation. But fewer elements decrease the correlation between the calculated CIR and the reference CIR. We use four elements in each group which reaches a good balance in the computational overhead and accuracy.

Comparing the method of using wired Tx and Rx to share the carrier frequency, our approach requires two data transmissions between Tx and Rx. The overhead incurred is acceptable as the data transmissions are between active wireless transceivers, and the SNR is typically orders of magnitude higher than that of the backscatter signal. We can use a very short duration packet between Tx and Rx to calculate h_E. In our implementation, the time for each packet is only 10 μs, and the total incurred time is less than $20 \cdot p + 10 \cdot \lceil p/4 \rceil = 0.68$ ms given $p = 30$ carrier frequencies and four frequencies in each group. LocRa has no special requirements on the form of the baseband signal, so it can be used in backscatter systems based on other wireless technologies. The idea of accurate estimate of the excitation signal channel can be even used in localization techniques for active devices [3].

4 TAG PHASE CALIBRATION

The Tx sends an excitation chirp to a LocRa tag which then shifts the frequency of the excitation chirp. As described in § 2, we estimate the channel of both the excitation signal and the backscatter signal, *i.e.,* $\hat{h_B}(f_c)$ and $\hat{h_E}(f_c)$. Considering the tag phase error, the channel estimation of the backscatter signal is $h_B(f_c) \cdot e^{j\Theta_{Tag}}$ instead of $h_B(f_c)$. We show how to address this problem in this section.

4.1 Uncertainty of Frequency Measurement

To address the tag phase error, the method in [8] measures the shifting frequency of the backscatter tag and then eliminate the phase offset based on the frequency. However, this faces two main challenges: (1) The shifting frequency is difficult to measure in a multipath environment; (2) The shifting frequency is unstable due to low-power oscillators on the backscatter tag. For challenge 1, assume the backscatter tag shifts the incident excitation signal by frequency Δf. Then, the backscatter signal arrives at Rx with different delays. By applying FFT to the dechirped signal, the peaks for the signal of different delays interfere with each other, resulting in a biased estimation of Δf. For challenge 2, even when the shifting frequency can be measured in advance, it varies across time due to severe jitter from the low-power oscillator. To verify the frequency jitter on backscatter tags, we design three types of tags with different crystal oscillators: the LTC6930 [34], LTC6907 [35] and an accurate signal generator AFG1022 [36]. We set their output frequency to 2 MHz and measure the actual frequency. Fig. 6 shows the CDF of instantaneous frequency jitter within 100 ms. The output frequency of LTC6930 has the highest jitter, varying from -35 Hz to 32 Hz. The LTC6907 is slightly better, varying from -13 Hz to 20 Hz. The external crystal oscillator on the signal generator AFG1022 has almost no jitter.

4.2 Phase Offset Cancellation

To accurately eliminate the phase offset, we transmit the excitation signal at the same carrier frequency twice and measure the channel $\hat{h}_1 = h \cdot e^{j\Theta_{tag}^1}$ and $\hat{h}_2 = h \cdot e^{j\Theta_{tag}^2}$. Those two excitation signals propagate through the same channel. The only difference is that the two signals are multiplied by the shifting frequency of different initial phases. Then, we can calculate the phase difference between two adjacent measurements, *i.e.,* $\Delta\Theta_{tag} = arg\left(\frac{\hat{h}_2}{\hat{h}_1}\right) = \Theta_{tag}^2 - \Theta_{tag}^1$. For the n^{th} channel measurement, we multiply it with $e^{-j(n-1)\Delta\Theta_{tag}}$. This allows us to recover the channel measurements at each carrier frequency to the same initial phase Θ_{tag}^1. This method works well when the shifting frequency is stable. However, in reality, the output frequency of the tag drifts as described in § 4.1. Assume the shifting frequency changes x Hz during the transmission of two adjacent carrier frequencies, and the duration of each signal is ΔT, then the actual phase offset caused by the tag is given by $\Delta\Theta'_{tag} = \Delta\Theta_{tag} + 2\pi \cdot x \cdot \Delta T$. If we calibrate the phase with the old $\Delta\Theta_{tag}$, then the phase error becomes $2\pi \cdot x \cdot \Delta T$. To see how the frequency drift affects the phase of channel measurements, we first measure the $\Delta\Theta_{tag}$ for the above three oscillators and use this value to calibrate the phase of the channel measurement within 100 ms. The phase error is shown in Fig. 7. The phase error of LTC6930 eventually accumulates to -6 radians, while that of LTC6907 is slightly smaller at 3.8 radians. In contrast, external crystal phase is very stable.

To address the problem of jitter in low-power oscillator on backscatter tags, we found that channels at the same carrier frequency should remain stable across multiple measurements. Leveraging this finding, we compensate for the frequency drift at different frequencies. For three carrier frequencies f_c^1, f_c^2, and f_c^3, the measured channels are $h(f_c^1) \cdot e^{j\Theta_{tag}^1}$, $h(f_c^2) \cdot e^{j\Theta_{tag}^2}$, $h(f_c^3) \cdot e^{j\Theta_{tag}^3}$,

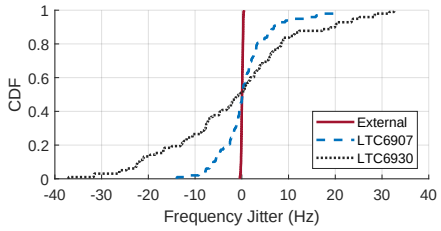

Figure 6: The output frequency of three different types of oscillator.

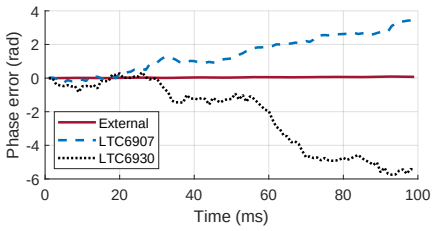

Figure 7: The phase error due to frequency drift.

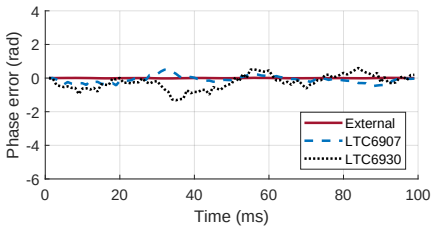

Figure 8: The phase error is eliminated in our approach.

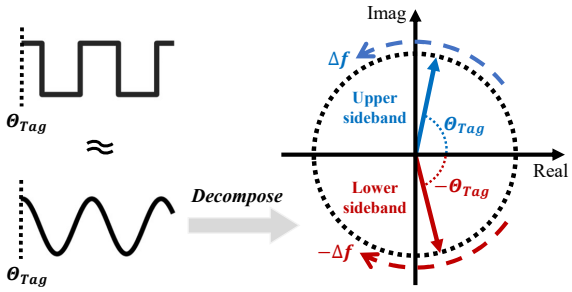

Figure 9: A square wave, approximated as a cosine wave, can be decomposed into two vectors rotating in opposite directions in the complex plane.

and $h(f_c^1) \cdot e^{j\Theta_{tag}^4}$. By removing the phase impact of Δf, we have $h(f_c^1) \cdot e^{j\Theta_{tag}^1}$, $h(f_c^2) \cdot e^{j(\Theta_{tag}^1 + 2\pi \cdot x \cdot \Delta T)}$, $h(f_c^3) \cdot e^{j(\Theta_{tag}^1 + 2\pi \cdot x \cdot 2\Delta T)}$, and $h(f_c^1) \cdot e^{j(\Theta_{tag}^1 + 2\pi \cdot x \cdot 3\Delta T)}$. We use the phase difference between the first and fourth channel measurement (*i.e.,* $2\pi \cdot x \cdot 3\Delta T$) to compensate the phase for f_c^2 and f_c^3. Note that the phase difference is the result of taking the modulo of 2π, meaning that the actual phase difference is $2\pi \cdot x \cdot 3\Delta T + k \cdot 2\pi$, where k is an integer. We should ensure that the phase difference is less than 2π. We calibrate the phase before the phase error exceeds 2π. For a crystal oscillator with a maximum frequency jitter of f_{jitter}, the minimum calibration time is $1/f_{jitter}$. For LTC6930 and LTC6907, the calibration time is 1/35 Hz = 28.6 ms and 1/20 Hz = 50 ms , respectively. Given a 4 ms excitation signal for each carrier frequency, we can calibrate tags equipped with LTC6930 and LTC6907 every 28.6 ms/4 ms ≈7 and 50 ms/4 ms ≈12 carrier frequencies respectively. As shown in Fig. 8, our calibration method significantly reduces the phase error. For LTC6930 and LTC6907, the average phase error within 100 ms is only 0.4 and 0.2 radians, respectively. To accommodate tags with unknown degree of jitter, we propose a calibration method in which the base station sends a training sequence in advance, measuring the tag's channel on a single frequency. However, due to the frequency jitter of the tag, we will get a channel measurement with a constantly changing phase value as shown in Fig. 7. The differential of the phase is the instantaneous frequency. We record the maximum instantaneous frequency in a period of time as f_{jitter}, and select the calibration frequency according to the phase accuracy of the specific application requirements, such as f_{jitter} or $2 \cdot f_{jitter}$, etc. LocRa does not require tag to perform more complex operations, so the power of tags is similar to that in other backscatter localization systems [8].

5 BANDWIDTH AND SNR IMPROVEMENT

As described in § 2.1, the localization accuracy depends on the bandwidth and SNR of the backscatter signal. We find that the backscatter signal can be divided into upper and lower sidebands in the frequency domain. In this section, we will introduce how to use this property to extend the bandwidth and improve the SNR of the backscattered signal, thereby enhancing localization accuracy.

5.1 Double Sidebands of Backscatter Signal

In § 2, we model the backscatter signal as a single-tone signal $e^{j(2\pi\Delta f t + \Theta_{Tag})}$. In practice, the backscatter signal is usually a square wave switching between two states. The square wave is also known as the reflection coefficient of the impedances, which can always be normalized to {-1, 1}. We consider the first harmonic of the square wave and approximate it as a cosine signal $cos(2\pi\Delta f t + \Theta_{Tag})$. As shown in Fig. 9, the signal on the complex plane can be decomposed into two vectors that rotate in opposite directions, *i.e.,* two single-tone signals of opposite frequencies: $e^{j(2\pi\Delta f t + \Theta_{Tag})}$ and $e^{-j(2\pi\Delta f t + \Theta_{Tag})}$. The signal of positive frequency is the upper sideband, and the signal of negative frequency is the lower sideband. Due to the symmetry of signal decomposition, the initial phases of two sidebands are opposite. We can rewrite the backscatter signal in Eq. 2 as:

$$\begin{aligned} S_B(t) &= S'(t) \cdot cos(2\pi\Delta f t + \Theta_{Tag}) \\ &= \underbrace{\frac{1}{2} S'(t) \cdot e^{j(2\pi\Delta f t + \Theta_{Tag})}}_{upper\ sideband} + \underbrace{\frac{1}{2} S'(t) \cdot e^{-j(2\pi\Delta f t + \Theta_{Tag})}}_{lower\ sideband} \end{aligned} \quad (20)$$

where $S'(t)$ is the exatation signal.

5.2 Virtual Bandwidth Extension

The backscatter signal in Eq. 20 is received and down-converted by the Rx. As the upper sideband signal and lower sideband signal have different frequencies, there are two peaks in the frequency domain. We can first eliminate the phase offset introduced by Tx, Rx, and tag using the method in § 3 and § 4. Assuming there is only one LoS path, similar to Eq. 5, the channel measurements of the upper sideband and lower sideband are $h_{upper}(f_c^i) = \alpha_1\alpha_2 \cdot e^{-j2\pi\Delta f \tau_2} \cdot e^{j\Theta_{tag}} \cdot e^{-j2\pi f_c^i(\tau_1+\tau_2)}$ and $h_{lower}(f_c^i) = \alpha_1\alpha_2 \cdot e^{-j2\pi(-\Delta f)\tau_2} \cdot e^{-j\Theta_{tag}} \cdot$

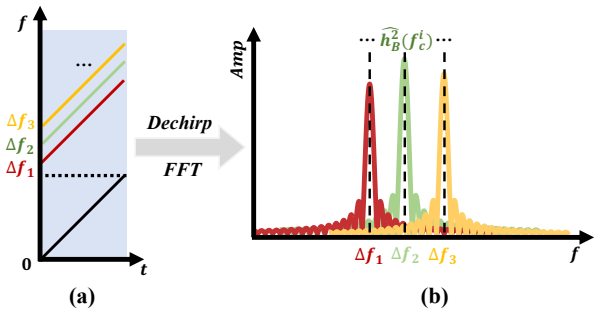

Figure 10: LocRa assigns different frequencies to different tags for parallel localization.

$e^{-j2\pi f_c^i(\tau_1+\tau_2)}$ where (α_1, τ_1) and (α_2, τ_2) are the (attenuation, delay) for Tx-to-Tag and Tag-to-Rx LoS path, respectively.

Applying IFFT to the channel estimation of the upper and lower sidebands, we will obtain two different CIRs: $f_{upper}(t) = \alpha_1\alpha_2 \cdot e^{-j2\pi\Delta f\tau_2}.e^{j\Theta_{tag}}.\delta(t-(\tau_1+\tau_2))$ and $f_{lower}(t) = \alpha_1\alpha_2.e^{-j2\pi(-\Delta f)\tau_2}.e^{-j\Theta_{tag}} \cdot \delta(t-(\tau_1+\tau_2))$. The time-domain CIRs for the upper sideband and lower sideband have two peaks of the same amplitude $\alpha_1\alpha_2$ but opposite phases: $-2\pi\Delta f\tau_2+\Theta_{tag}$ and $-2\pi(-\Delta f)\tau_2-\Theta_{tag}$. If we directly combine the CIR of the upper and lower sidebands, the derived CIR may be coherently canceled and distorted. To utilize the channel measurements of the upper and lower sidebands, we propose a method to ensure the coherent enhancement of CIR.

$$\begin{aligned}\left[h_{lower}\left(f_c^i\right)\right]^* &= \alpha_1\alpha_2 \cdot e^{-j2\pi\Delta f\tau_2} \cdot e^{j\Theta_{tag}} \cdot e^{-j2\pi\left(-f_c^i\right)(\tau_1+\tau_2)} \\ &= h_{upper}\left(-f_c^i\right)\end{aligned} \tag{21}$$

We first calculate the conjugate of the lower sidebands as in Eq. 21. The conjugate of the channel measurement of the lower sideband is equivalent to re-measure the channel of the upper sideband at the corresponding negative frequency. For example, if we measure the channel at 2.4GHz~2.5GHz, we obtain the channel measurement at -2.5GHz~-2.4GHz by calculating the conjugated values.

After obtaining the channel estimation of the negative frequency, we cannot directly use the IFFT to obtain the CIR as the mixed channel estimation is discontinuous in the frequency domain (e.g., 2.4GHz~2.5GHz and -2.5GHz~-2.4GHz). To deal with a non-uniformly spaced channel estimation sequence, we use the Inverse Non-uniform Discrete Fourier Transform (INDFT) [37] to infer the time domain impulses. Previous work [3] proposed a learning-based method to solve the INDFT problem. We leverage this method and apply INDFT to hybrid and discontinuous channel estimation sequence, and obtain CIR with higher accuracy.

Our method improves localization accuracy from two aspects: First, using double sidebands helps to average the noise and improves the SNR of the time domain pulse since the backscatter signal is usually very weak. Second, re-measuring the channel at the negative frequency virtually improves the bandwidth of the backscatter signal, which enhances the ability to distinguish multipath.

6 MULTIPLE TAGS LOCALIZATION

LocRa enables backscatter localization over a range of tens of meters using multiple backscatter tags. We propose a frequency division multiple access (FDMA) technique to distinguish different backscatter tags in the localization process. Specifically, we assign distinct frequency shifts to individual tags, denoted as Δf_l for tag l. Subsequently, tags shift the frequency of the excitation signal at the assigned frequencies as described Eq. 2. This enables the separation of signals for different tags in the frequency domain, as illustrated in Fig. 10(a). After dechirping, the backscatter signals of different frequency shifts transform into different single-frequency signals that can be identified through FFT analysis. The peaks of different frequencies fall on different FFT bins, and we can obtain the channel state information of the corresponding tags by recording the value of the corresponding peak, as illustrated in Fig. 10(b).

However, this method can cause the interference problem between tags. When two shifting frequencies are close, in FFT domain, the sidelobe of the peak of one tag will interfere with the peaks corresponding to other tags. As shown in Fig. 10(b), those three tags have three main lobes at their corresponding shifting frequencies. Meanwhile, they also have side lobes with a certain height, which can interfere with the main lobes of other tags. More parallel tags can cause more interference among them due to more energy in the sidelobes. In addition, a tag with a higher power also has high sidelobes that is more likely to interfere with other nearby tags.

We use the energy equalization method and the window function method in the existing parallel backscatter communication to solve this problem. Netscatter [24] has observed that adjacent peaks in the frequency domain having the similar amplitude can reduce interference between them. Therefore, we measure the signal strength of each tag and attenuate the excitation signal to a corresponding level for tags with high energy, ensuring that the reflected signals of all tags have similar amplitudes. In addition, PPLoRa [23] employs a Hanning window to mitigate signal interference between backscatter tags. A Hanning window has a decreasing amplitude from the center to both ends, which effectively reduces the height of sidelobes caused by finite length signal in FFT. While both methods can reduce interference between tags, the number of parallel tags and the frequency difference between two adjacent allocated frequencies still affect localization accuracy. We evaluate the impact of these two factors in § 8.1.6.

7 IMPLEMENTATION

Base Stations. We implement LocRa base stations on three USRP N210 [38]. We implement the synchronization algorithm of LocRa through the C++ interface provided by UHD [39]. LocRa requires the calibration of the phase for distributed base station by exchanging data packets, which necessitates that the same transceiver shares the carrier frequency during transmission and reception. However, the UBX40 daughterboard installed in USRP N210 utilizes two distinct RF links that use asynchronous carriers. We found that the UBX40 can operate in full-duplex mode, in which it can receive while transmitting and record the phase of the signal leaked from the transmitting link. This enables the pre-calibration of the carrier phase of the same base station. The signal sampled by the USRP is stored in a file, and is then processed in MATLAB. After

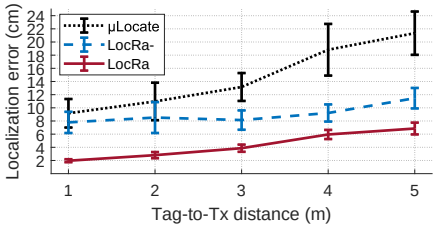

Figure 11: Short-range benchmark.

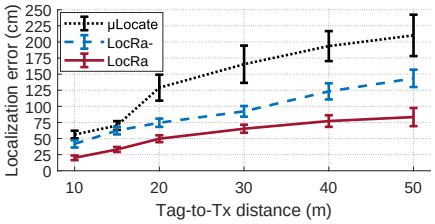

Figure 12: Long-range benchmark.

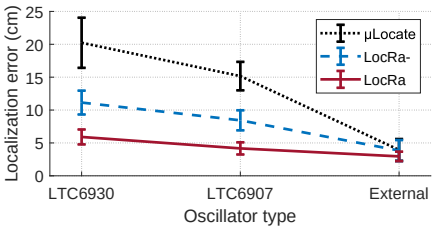

Figure 13: Localization error with different oscillators.

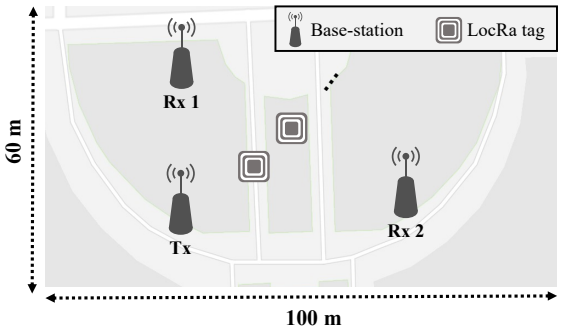

Figure 14: Benchmark experimental map.

channel estimation, we perform the bandwidth extension method and INDFT algorithm in python.

LocRa Backscatter Tags. We prototype the LocRa backscatter tag with three components: an RF switch, a low-power programmable oscillator, and a power module. We use an ADG902 RF switch [40], which is directly controlled by the output of the oscillator. We build three prototypes with different oscillators, namely LTC6907 [35], LTC6930-8.00 [34], and an external signal generator AFG1022 [36]. The total power consumption is 303 μW. We set the frequency of all those oscillators to 2 MHz.

8 EVALUATION

8.1 Micro Benchmark

We evaluate the localization performance of LocRa and compare it with previous work μlocate, the state-of-the-art LoRa backscatter localization system with Tx and Rx synchronization. In μlocate, we implement a concurrent transmission based method to compensate the tag phase drift. Otherwise, it has a very large localization error due to the tag phase drift. To fully evaluate the performance, we implement a version of LocRa without double sideband signal bandwidth extension, namely LocRa-.

8.1.1 Basic localization experiment. We first conduct short-range experiments in an open field. We place the Tx in one corner of a square and two Rx on the two corners adjacent to Tx. Then, we gradually move the tag along the diagonal of the square starting from the Tx. The experimental map and equipment layout are shown in Fig. 14. The distance between the Tx and Rx is fixed to 5 m. The transmit power of Tx is 20 dBm. We use the 2.4 GHz to 2.5 GHz band, and the total bandwidth is 100 MHz. We record the localization error with different Tx-to-tag distances from 1 m to 5 m.

As shown in Fig. 11, the localization error of LocRa is 1.9 cm when the Tx-to-tag distance is 1 m. As the tag moves away from Tx, the localization error of LocRa increases. When the Tx-to-tag distance is 5 m, the error is 6.8 cm. At 5 m, the error of LocRa- and μlocate reaches 11.4 cm and 21.3 cm, respectively. Among those systems, LocRa achieves the best localization performance. Compared with LocRa-, LocRa improves the localization accuracy in the following two aspects. First, it combines the double sidebands to expand the bandwidth and enhances the ability to separate multipath. Second, it coherently adds the upper and lower sideband signals to improve the SNR. Thus, LocRa can obtain more accurate time domain impulse.

μlocate does not accurately estimate and calibrate the phase offset caused by the tag, resulting in a larger localization error. It is worth noting that μlocate has a similar performance to LocRa- when Tx-to-tag distance is 1 m and 2 m. But when the Tx-to-tag distance increases to 4 m, the localization error of μlocate rises rapidly. This is because when the SNR of the backscatter signal is high, μlocate can measure the channel of the backscatter signal by concurrently transmitting multiple frequency bands. Thus, it can reduce the effect of the tag phase drift over time. However, according to FCC regulations and the physical limitations of common wireless transmitters, measuring at multiple frequencies concurrently will reduce the energy of each signal and thereby reduce the SNR. Thus, the increase in the Tx-to-tag distance reduces the accuracy of tag phase drift estimation. When the Tx-to-tag distance is 4 m, it can only measure on eight frequencies concurrently, while at 1 m and 2 m, this number is 18 and 14, respectively.

8.1.2 Long-range experiment. The experimental field and layout of the Tx, Rx, and tag are the same as above. We set the distance between Tx and Rx to 48 m. We use 25 MHz bandwidth centered on 433 MHz to avoid the higher attenuation for the 2.4 GHz band. Tx is connected to a power amplifier, and transmits at 30 dBm. Then, we record the localization error of a tag with different Tx-to-tag distances from 10 m to 50 m.

Fig. 12 shows that LocRa outperforms the other two methods. As the distance increases, the localization error of all three methods increases. At 10 m and 15 m, μlocate can still maintain a similar error to LocRa-. As the distance further increases, the signal SNR also decreases and the number of excitation signals that can be concurrently transmitted also decreases. Finally, at 50 m, the error

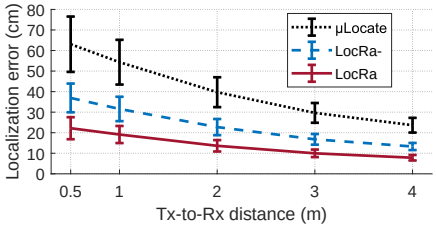

Figure 15: Localization error with different Tx-to-Rx distance.

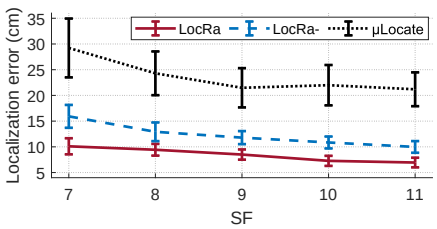

Figure 16: Localization error with different SF (short-range).

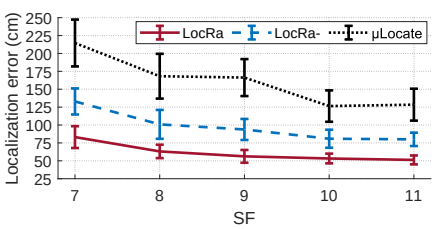

Figure 17: Localization error with different SF (long-range).

of μlocate is 2.1 m and the error of LocRa- is 1.4 m. LocRa further reduces the error to 88 cm. LocRa concentrates the energy of the backscatter signal in the time domain to achieve localization distance similar to those of μlocate. However, LocRa improves accuracy of μlocate by eliminating phase jitter of the tag and utilizing both the upper and lower sidebands. As a result, LocRa achieves significantly lower localization errors at various distances. We observe that the improvement of LocRa over LocRa- increases with increasing of the Tx-to-tag distance. This indicates that the combination of the upper and lower sidebands can significantly improve the localization accuracy especially when the SNR is low. Moreover, the inter-base station synchronization algorithm employed by LocRa significantly simplifies the deployment process for long-range localization. Note that the distance between base stations in our experiment is 48 m. In such a scenario, using RF cable for synchronization would be impractical.

8.1.3 Impact of different oscillators. We notice that the performance of our implementation of μlocate is lower than that in their paper. The localization error is 14 cm when the Tx-to-tag distance is 5 m. One of the main error sources is the tag phase drift over time. The phase drift of different oscillators varies significantly. Thus, we measure the localization errors of those three systems under different oscillators mentioned in § 4.1. We fix the position of Tx, Rx, and tag in a room and keep the surrounding environment stable. For each oscillator, we evaluate those three localization algorithms and calculate the error.

Fig. 13 shows the localization error. Due to frequency drift of LTC6930, the localization error of μlocate reaches 20.2 cm, while the localization error of LocRa- and LocRa is only 11.1 cm and 5.9 cm, respectively. With more stable LTC6907, the localization error of μlocate decreases to 15.1 cm. Both LocRa and LocRa- have lower localization errors. With an external high-precision oscillator, the localization error of μlocate and LocRa- becomes similar, which are 3.9 cm and 3.8 cm, respectively. Since LocRa uses both upper and lower sidebands, the error further decreases to 2.9 cm. The results show that LocRa can work under different quality oscillators. This enhances the practicality of the backscatter localization system because instable crystal oscillators (e.g., LTC6930) are widely used in existing backscatter communication systems [23]. LocRa is able to be deployed in those tags and works well. μlocate achieves similar performance to that of LocRa- under high-precision oscillators. Its performance decreases rapidly with a higher jitter oscillator. In our experiments, we use LTC6907 in our tag.

8.1.4 Impact of distance between Tx and Rx. To verify the benefits of distributed placement of Tx and Rx, we fix the Tx-to-tag distance to 5 m and continuously increase the Tx-to-Rx distance. We measure the localization error at different Tx-to-Rx distances. As shown in Fig. 15, the localization error gradually decreases as the distance between Tx and Rx increases. As LocRa does not require additional external clock and RF cables for synchronization, the deployment of Tx and Rx can be more flexible. LocRa can support Tx and Rx with a large distance. Thus, it can work for the COTS LoRa network infrastructure.

8.1.5 Impact of SF. We explore the effect of SF on localization accuracy for both short and long distances. In the short-range experiment, we fix both the Tx-to-Rx distance and the Tx-to-tag distance to 5 m. In the long-range experiment, we fix the Tx-to-Rx distance to 48 m and the Tx-to-tag distance to 20 m. Then, we change the SF of the excitation signal from SF7 to SF11 and measure the localization error.

As shown in Fig. 16 and 17, the SF of the backscatter signal affects the SNR of the channel measurement and therefore the localization accuracy. For μlocate, a lower SNR will distort the measurement of the shifting frequency of the tag, thus reducing the accuracy of tag phase offset measurement. Fig. 16 shows the performance of SF10 and Fig. 17 shows that of SF9. It is worth noting that as SF increases, μlocate does not necessarily performs better. This is because although the increase of SF improves the SNR, the localization delay also increases which increases the accumulated phase offset. For LocRa and LocRa-, a smaller SF also causes more phase noise in calibrating the phase of the tag. LocRa- and LocRa perform fine-grained phase calibration for the tag. Thus, the localization accuracy is not affected after increasing localization delay. LocRa utilizes both the upper and lower sidebands signal, and thus it improves the localization accuracy under all SF. At SF7, the localization error of μlocate, LocRa-, and LocRa is 29.2 cm, 15.9 cm, and 10.1 cm in the short-range experiment. In this setting, LocRa achieves the largest improvement among all SF. This is because the SNR of channel measurements is very low at SF7; thus, the SNR becomes the bottleneck. LocRa utilizes double sidebands, and the improvement is more obvious under such a scenario. Also, the accuracy improvement of LocRa is higher in long-range experiments in general because of lower SNR and more complex multipath.

8.1.6 Multiple tags localization. We conduct a trace-based simulation experiment to verify the effect of LocRa when multiple tags are located simultaneously. We first pre-allocate the corresponding shifting frequency to tags, starting from 2 MHz and increasing by

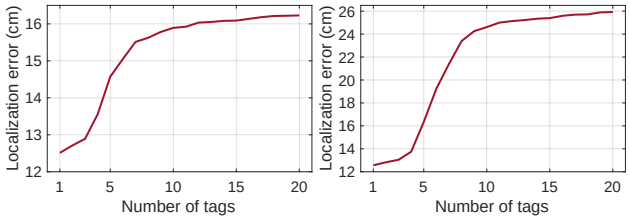

(a) 1 kHz (b) 0.5 kHz

Figure 18: Localization error for multiple tags

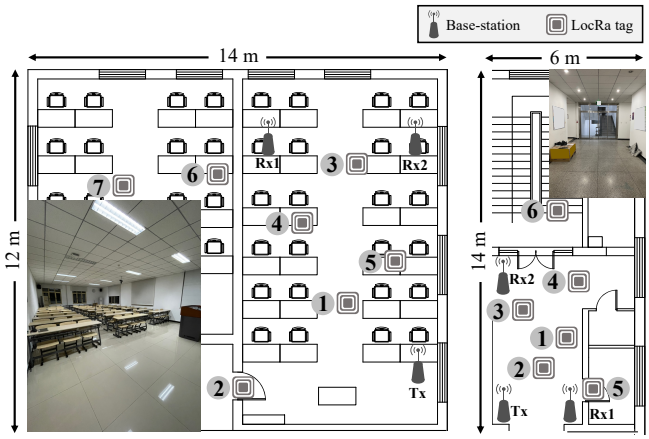

(a) Classroom (b) Hallway

Figure 19: Floor map of the classroom and hallway.

1 kHz for each tag. Then, we keep adding tags to the network. Every time adding a new tag, we measure the average localization error of all tags. There are 20 tags in total. In the experiment, all tags are placed close to each other, and the power normalization method is used to make the backscatter signal energy of different tags similar. As shown in Fig. 18(a), the localization error slowly increases with increasing of tags and eventually becomes stable at around 16 cm.

Adjacent allocated shifting frequency is also an important parameter in multi-tag case. It determines the number of tags that the system can accommodate for simultaneous localization. Therefore, we change the adjacent shifting frequency to 0.5 kHz to measuring the localization accuracy of LocRa. As shown in Fig. 18(b), the localization error only rises to 26 cm, which shows that LocRa can work under different shifting frequencies. Users can choose the shifting frequency according to the network scale and expected localization accuracy.

8.2 Real World Scenarios

To evaluate the localization accuracy of LocRa in real scenarios, we deploy LocRa in classrooms and a hallway and measure the localization error of LocRa in various locations. The output power of the Tx is 20 dBm.

8.2.1 Classroom. Fig. 19(a) shows the layout of the two classrooms and the placement of tags and base stations. Two classrooms are separated by a wall of concrete and wood planks. In each classroom, tables, chairs, and lecterns are densely placed. We fix the Tx and two Rx in the corners of the same classroom. One Rx is 5 m away from Tx, and the other is 8 m from Tx. We place the tag at different locations in those two classrooms.

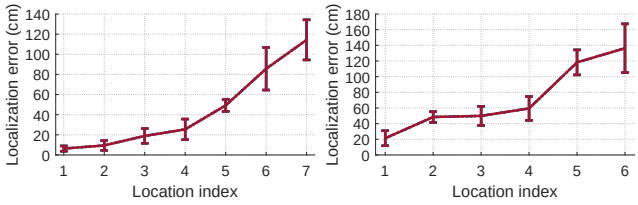

(a) Classroom (b) Hallway

Figure 20: Localization error in real scenarios

As shown in Fig. 20(a), the localization error in the right classroom varies from 6 cm to 49 cm. In the indoor environment, the multipath environment is more complex. The superposition of different paths distorts the CIR and thus reduces the accuracy of measuring the LoS path. LocRa can achieve centimeter-level to decimeter-level localization accuracy in the room. In the left room, multipath environment becomes more complex, and the SNR further decreases as the backscatter signal needs to pass through a wall. The location error is 85 cm and 114 cm at locations 6 and 7, respectively.

8.2.2 Hallway. Fig. 19(b) shows the layout and placement of base stations. The distance between the two Rx and Tx is 3.5 m and 7 m, respectively. We place the tag in six different locations, two of which are in the equipment room with metal cabinets and the stairwell.

Fig. 20(b) shows that the localization error in different locations varies from 21 to 136 cm. The localization accuracy in the hallway is generally lower than that in the classroom. This is because the hallway is a narrower area than the classroom, and it is likely to have more reflections from the walls. The localization error at position 5 is relatively higher than the errors at the adjacent positions 1 and 2. This is because multiple cabinets are placed directly behind the tag at position 5, and the signal from this strong reflection path distorts the LoS time-domain impulse. In summary, LocRa can achieve a high localization accuracy in different multipath indoor environments.

9 RELATED WORKS

Wireless localization. There are many research works on wireless localization due to its great potential in commercial and industrial applications. Spotfi [4] proposes a super-resolution AoA estimation algorithm from CSI of multiple WIFI APs. Chronos [3] makes a transmitter and receiver hop between different frequency bands to compute sub-nanosecond time-of-flight. Splicer [11] derives high-resolution power delay profiles by splicing the CSI measurements from multiple WiFi frequency bands. MonoLoco [41] exploits the multipath triangulation algorithm and WiFi CSI values from an antenna array to localize another WiFi device. Besides localization for active transceivers, the localization of passive backscatter tags

has also attracted much research interest. RFind [5] and TurboTrack [6] emulate a large bandwidth of the reflected signal from the RFID tag to perform 3D localization with sub-centimeter accuracy. However, these systems can only work within a limited range (2-5m). In order to extend the working range of wireless localization, a new approach is to use spread spectrum signals, such as LoRa. Owll [42] develops a distributed base station network that together spans a wide bandwidth to localize LoRa clients. Seirios [7] synchronizes multiple non-overlapped communication channels to increase the overall bandwidth. μlocate [8] and Marvel [13] provide the LoRa backscatter localization with high accuracy. Those approaches cannot work for distributed based stations.

Backscatter communication. Ambient backscatter [43] uses ambient broadcast TV or cellular signals as the excitation signal for device-to-device communication. FM backscatter [44] reflects the ambient FM signals and conveys backscatter data on it. Wi-Fi backscatter [45] transmits information by changing the RSSI of Wi-Fi packets. BackFi [46] changes the channel between the Wi-Fi transceivers to convey data bits. Interscatter [27] uses a single frequency signal sent by a commercial BLE device and generates Wi-Fi signal over it. Hitchhike [26] convey data on an ambient Wi-Fi packet by translating the excitation Wi-Fi codeword to another valid codeword. WiTag [47] selectively corrupts some subframes of a Wi-Fi packet and realizes backscatter communication based on whether the ACK packet sent by the receiver can be correctly decoded. TScatter [48] uses high-granularity sample-level modulation to avoid the phase offset from tags and thus reduces the BER. IBLE [28] uses instantaneous phase shift modulation and FEC coding to improve the reliability of BLE backscatter communication. SD-PHY [49] change the amplitude and phase of the backscatter signals to comply with various wireless protocols. To improve the communication range, LoRa technology has been exploited in backscatter communication. LoRea [50] achieves thousands of meters of backscatter communication distance by frequency shifting the signal out of the band. PLoRa [22] uses two baseband signals to shift the excitation chirp and splice them to form a new backscatter chirp. FlipTracer [51] separates collided RFID packets using a transition probabilities model. TaGroup [52] proposes a RFID grouping technique based on proximity relations between tags. LoRa backscatter [25] and Netscatter [24] use a single-tone frequency as the excitation signal. The tag then modulates the incident signal to a chirp. P^{2}LoRa [23] allocates different shifting frequencies to multiple tags and implements an ambient backscatter system with parallel decoding.

10 CONCLUSION

We propose LocRa, the first localization system for long-range backscatter tags with distributed single antenna base stations. LocRa can work with existing infrastructure of distributed base stations and low-power tags. We exploit the excitation signal to measure the precise channel between base stations and then use this to calibrate random errors in backscatter signals. We propose a method for calibration of backscatter tags and address the phase drifting introduced by low-power tags. Finally, we use the upper and lower double-sidebands to expand the bandwidth and improve the SNR. We prototype LocRa tags using customized hardware and implemented LocRa base stations on USRP. We perform extensive experiments to evaluate the performance. The localization error is only 6.8 cm and 88 cm, respectively When the LocRa tag is 5 m and 50 m away from the base station, Compared with the state-of-the-arts, LocRa achieves 3.1× and 2.3× higher localization accuracy.

11 ACKNOWLEDGMENTS

This work is in part supported by National Key R&D Program of China 2022YFC3801300, National Natural Science Foundation of China (U22A2031, No. 61932013, 62172250). Jiliang Wang is the corresponding author.

REFERENCES

[1] Yuxiang Lin, Wei Dong, Yi Gao, and Tao Gu. SateLoc: A virtual fingerprinting approach to outdoor LoRa localization using satellite images. *ACM Transactions on Sensor Networks (TOSN)*, 17(4):1–28, July 2021.
[2] Atul Bansal, Akshay Gadre, Vaibhav Singh, Anthony Rowe, Bob Iannucci, and Swarun Kumar. OwLL: Accurate LoRa Localization using the TV Whitespaces. In *Proceedings of ACM/IEEE IPSN*, 2021.
[3] Deepak Vasisht, Swarun Kumar, and Dina Katabi. Decimeter-Level localization with a single WiFi access point. In *Proceedings of USENIX NSDI*, 2016.
[4] Manikanta Kotaru, Kiran Joshi, Dinesh Bharadia, and Sachin Katti. Spotfi: Decimeter level localization using wifi. In *Proceedings of ACM SIGCOMM*, 2015.
[5] Yunfei Ma, Nicholas Selby, and Fadel Adib. Minding the billions: Ultra-wideband localization for deployed rfid tags. In *Proceedings of ACM MobiCom*, 2017.
[6] Zhihong Luo, Qiping Zhang, Yunfei Ma, Manish Singh, and Fadel Adib. 3d backscatter localization for fine-grained robotics. In *Proceedings of USENIX NSDI*, 2019.
[7] Jun Liu, Jiayao Gao, Sanjay Jha, and Wen Hu. Seirios: Leveraging Multiple Channels for LoRaWAN Indoor and Outdoor Localization. In *Proceedings of ACM MobiCom*, 2021.
[8] Rajalakshmi Nandakumar, Vikram Iyer, and Shyamnath Gollakota. 3d localization for sub-centimeter sized devices. In *Proceedings of ACM Sensys*, 2018.
[9] SEMTECH. LoRa applications. https://www.semtech.com/lora/lora-applications.
[10] Suraj Jog, Junfeng Guan, Sohrab Madani, Ruochen Lu, Songbin Gong, Deepak Vasisht, and Haitham Hassanieh. Enabling IoT Self-Localization Using Ambient 5G Signals. In *Proceedings of USENIX NSDI*, 2022.
[11] Yaxiong Xie, Zhenjiang Li, and Mo Li. Precise power delay profiling with commodity wifi. In *Proceedings of ACM MobiCom*, 2015.
[12] Alexander Canals, Pascal Josephy, Simon Tanner, and Roger Wattenhofer. Robust indoor localization with ADS-B. In *Proceedings of ACM Mobicom*, 2021.
[13] Shengkai Zhang, Wei Wang, Ning Zhang, and Tao Jiang. Rf backscatter-based state estimation for micro aerial vehicles. In *Proceedings of IEEE INFOCOM*, 2020.
[14] Jingxian Wang, Vaishnavi Ranganathan, Jonathan Lester, and Swarun Kumar. Ultra low-latency backscatter for fast-moving location tracking. In *Proceedings of ACM UbiComp*, 2022.
[15] Elahe Soltanaghaei, Akarsh Prabhakara, Artur Balanuta, Matthew Anderson, Jan M Rabaey, Swarun Kumar, and Anthony Rowe. Millimetro: mmwave retro-reflective tags for accurate, long range localization. In *Proceedings of ACM MobiCom*, 2021.
[16] Elahe Soltanaghaei, Adwait Dongare, Akarsh Prabhakara, Swarun Kumar, Anthony Rowe, and Kamin Whitehouse. Tagfi: Locating ultra-low power wifi tags using unmodified wifi infrastructure. In *Proceedings of ACM UbiComp*, 2021.
[17] Jie Xiong, Karthikeyan Sundaresan, and Kyle Jamieson. Tonetrack: Leveraging frequency-agile radios for time-based indoor wireless localization. In *Proceedings of ACM MobiCom*, 2015.
[18] Ettus Research. GPSDO. https://www.ettus.com/all-products/gpsdo-mini/.
[19] Kubra Alemdar, Divashree Varshney, Subhramoy Mohanti, Ufuk Muncuk, and Kaushik Chowdhury. Rfclock: timing, phase and frequency synchronization for distributed wireless networks. In *Proceedings of ACM Mobicom*, 2021.
[20] Omid Abari, Hariharan Rahul, Dina Katabi, and Mondira Pant. Airshare: Distributed coherent transmission made seamless. In *Proceedings of IEEE INFOCOM*, 2015.
[21] Ali Najafi and Michael Wei. Graham: Synchronizing clocks by leveraging local clock properties. In *Proceedings of USENIX NSDI*, 2022.
[22] Yao Peng, Longfei Shangguan, Yue Hu, Yujie Qian, Xianshang Lin, Xiaojiang Chen, Dingyi Fang, and Kyle Jamieson. PLoRa: A passive long-range data network from ambient LoRa transmissions. In *Proceedings of ACM SIGCOMM*, 2018.
[23] Jinyan Jiang, Zhenqiang Xu, Fan Dang, and Jiliang Wang. Long-range ambient LoRa backscatter with parallel decoding. In *Proceedings of ACM Mobicom*, 2021.

[24] Mehrdad Hessar, Ali Najafi, and Shyamnath Gollakota. Netscatter: Enabling large-scale backscatter networks. In *Proceedings of USENIX NSDI*, 2019.

[25] Vamsi Talla, Mehrdad Hessar, Bryce Kellogg, Ali Najafi, Joshua R Smith, and Shyamnath Gollakota. LoRa backscatter: Enabling the vision of ubiquitous connectivity. In *Proceedings of ACM UbiComp*, 2017.

[26] Pengyu Zhang, Dinesh Bharadia, Kiran Joshi, and Sachin Katti. Hitchhike: Practical backscatter using commodity WiFi. In *Proceedings of ACM Sensys*, 2016.

[27] Vikram Iyer, Vamsi Talla, Bryce Kellogg, Shyamnath Gollakota, and Joshua Smith. Inter-technology backscatter: Towards internet connectivity for implanted devices. In *Proceedings of ACM SIGCOMM*, 2016.

[28] Maolin Zhang, Si Chen, Jia Zhao, and Wei Gong. Commodity-level BLE backscatter. In *Proceedings of ACM MobiSys*, 2021.

[29] Pengyu Zhang, Mohammad Rostami, Pan Hu, and Deepak Ganesan. Enabling practical backscatter communication for on-body sensors. In *Proceedings of the ACM SIGCOMM*, 2016.

[30] Renjie Zhao, Fengyuan Zhu, Yuda Feng, Siyuan Peng, Xiaohua Tian, Hui Yu, and Xinbing Wang. OFDMA-enabled Wi-Fi backscatter. In *Proceedings of ACM MobiCom*, 2019.

[31] Hariharan Rahul, Haitham Hassanieh, and Dina Katabi. Sourcesync: A distributed wireless architecture for exploiting sender diversity. In *Proceedings of ACM SIGCOMM*, 2010.

[32] Ezzeldin Hamed, Hariharan Rahul, Mohammed A Abdelghany, and Dina Katabi. Real-time distributed mimo systems. In *Proceedings of ACM SIGCOMM*, 2016.

[33] Maxime Guillaud, Dirk TM Slock, and Raymond Knopp. A practical method for wireless channel reciprocity exploitation through relative calibration. In *Proceedings of ISSPA*, 2005.

[34] Analog Devices. LTC6930. https://www.analog.com/media/en/technical-documentation/data-sheets/6930fe.pdf.

[35] Analog Devices. LTC6907. https://www.analog.com/media/en/technical-documentation/data-sheets/6907fa.pdf.

[36] Tektronix. AFG1022. https://www.tek.com/en/arbitrary-function-generator/afg1000-manual.

[37] Sonali Bagchi and Sanjit K Mitra. *The nonuniform discrete Fourier transform and its applications in signal processing*, volume 463. Springer Science & Business Media, 2012.

[38] Etuss Research. USRP N210. https://www.ettus.com/all-products/un210-kit/.

[39] Etuss Research. UHD. https://files.ettus.com/manual/.

[40] Analog Devices. ADG902. https://www.analog.com/media/en/technical-documentation/data-sheets/ADG901_902.pdf.

[41] Elahe Soltanaghaei, Avinash Kalyanaraman, and Kamin Whitehouse. Multipath Triangulation: Decimeter-Level WiFi Localization and Orientation with a Single Unaided Receiver. In *Proceedings of ACM MobiSys*, 2018.

[42] Atul Bansal, Akshay Gadre, Vaibhav Singh, Anthony Rowe, Bob Iannucci, and Swarun Kumar. OwLL: Accurate LoRa Localization Using the TV Whitespaces. In *Proceedings of ACM IPSN*, 2021.

[43] Vincent Liu, Aaron Parks, Vamsi Talla, Shyamnath Gollakota, David Wetherall, and Joshua R Smith. Ambient backscatter: Wireless communication out of thin air. In *Proceedings of ACM SIGCOMM*. ACM, 2013.

[44] Anran Wang, Vikram Iyer, Vamsi Talla, Joshua R Smith, and Shyamnath Gollakota. FM backscatter: Enabling connected cities and smart fabrics. In *Proceedings of USENIX NSDI*, 2017.

[45] Bryce Kellogg, Aaron Parks, Shyamnath Gollakota, Joshua R Smith, and David Wetherall. Wi-Fi backscatter: Internet connectivity for RF-powered devices. In *Proceedings of ACM SIGCOMM*, 2014.

[46] Dinesh Bharadia, Kiran Raj Joshi, Manikanta Kotaru, and Sachin Katti. Backfi: High throughput wifi backscatter. In *Proceedings of ACM SIGCOMM*, 2015.

[47] Ali Abedi, Farzan Dehbashi, Mohammad Hossein Mazaheri, Omid Abari, and Tim Brecht. Witag: Seamless wifi backscatter communication. In *Proceedings of ACM SIGCOMM*, 2020.

[48] Xin Liu, Zicheng Chi, Wei Wang, Yao Yao, Pei Hao, and Ting Zhu. Verification and Redesign of OFDM Backscatter. In *Proceedings of USENIX NSDI*, 2019.

[49] Fengyuan Zhu, Mingwei Ouyang, Luwei Feng, Yaoyu Liu, Xiaohua Tian, Meng Jin, Dongyao Chen, and Xinbing Wang. Enabling software-defined phy for backscatter networks. In *Proceedings of ACM MobiSys*, 2022.

[50] Ambuj Varshney, Oliver Harms, Carlos Pérez-Penichet, Christian Rohner, Frederik Hermans, and Thiemo Voigt. LoRea: A backscatter architecture that achieves a long communication range. In *Proceedings of ACM Sensys*, 2017.

[51] Meng Jin, Yuan He, Xin Meng, Yilun Zheng, Dingyi Fang, and Xiaojiang Chen. Fliptracer: Practical parallel decoding for backscatter communication. In *Proceedings of ACM MobiCom*, 2017.

[52] Meng Jin, Kexin Li, Xiaohua Tian, Xinbing Wang, and Chenghu Zhou. Fast, fine-grained, and robust grouping of RFIDs. In *Proceedings of ACM MobiCom*, 2023.